Proceedings of the 21st ICSMGE, Vienna, Austria, 14 – 19 June 2026. Pistrol, Adam & Schweiger (eds.)
Published by: ÖGG, Austrian Society for Geomechanics, Salzburg, Austria, ISBN 978-3-9503898-4-5
https://doi.org/10.53243/ICSMGE2026-1455

Monitoring and modelling of rock mass stability considering thermal and mechanical effects: a case study at Capanna Margherita, Monte Rosa

Yunlu Bai, Francesco Calvetti
Department of Architecture, Built Environment and Construction Engineering, Politecnico di Milano, Milan, Italy, yunlu.bai@polimi.it

Andrea Tamburini
IMAGEO, Milan, Italy

ABSTRACT: Climate change is triggering, among other effects, permafrost degradation, which poses significant threats to the stability of rock slopes in high-altitude regions such as the Alps. Previous studies have shown that in the Alps, rockfall and rock/ice avalanche events are more frequent within the altitude range where the mean annual rock surface temperature is around 0 °C, i.e. where permafrost degradation occurs due to several mechanisms including decreased ice resistance, repeated frost-thaw cycles, and thermal-induced deformation. This study investigates the mechanical response of high-altitude rock slopes by integrating field monitoring and numerical simulations. The research is conducted at Capanna Margherita, the highest hut in Europe, located on Punta Gnifetti of Monte Rosa (4554 m a.s.l.). The project began in September 2023 when two multiparametric DMS (Differential Monitoring of Stability) columns were installed in the rock mass. DMS modules are equipped with thermometer, 3D accelerometer, inclinometer, extensometer, and piezometer. Numerical analyses are performed on a 3D Distinct Element model, which reproduces the geo-structural setting of Punta Gnifetti, with the slope profile derived from a 3D point cloud obtained by photogrammetry and laser scanning. Joint families are defined from a statistical interpretation of the point cloud and direct detection in the borehole using an optical televiewer. A series of preliminary simulations has been conducted to assess the influence of joint persistence and its relationship with joint resistance at the slope scale. The model is then used to study scenarios of rock slope degradation by progressively reducing joint resistance. The comparison between simulations and monitoring data suggests that the deformation recorded in the borehole involves both mechanical and thermal responses. Although the preliminary findings require further long-term validation, particularly regarding irreversible effects, they highlight the mechanical failure mechanisms and lay the foundation for developing a thermo-mechanical coupled model of high-altitude rock slopes.

KEYWORDS: DEM model, rock mass, slope stability, in-situ monitoring, high Alps.

1 INTRODUCTION

Rockfalls and rockslides are becoming a common hazard in the Alps, with increasing frequency in the 21st century, particularly in high-altitude areas (Ravanel et al., 2017). Their impact on infrastructure (mountain huts, transportation facilities) and human activity is a growing concern.

Research aimed at unravelling the mechanisms that weaken high-Alpine rock slopes and walls now draws on a network of instrumented sites across the European Alps, where borehole monitoring provides the most direct and fundamental evidence of thermo-mechanical change. Multi-depth thermistor strings reveal an accelerated warming signal: a pan-Alpine synthesis of 64 boreholes (2400-3900 m a.s.l.) reports >1 °C per decade at 10 m depth for 2013-2022, with the fastest rates at cold, ice-poor bedrock sites (Noetzli et al., 2024). Region-specific records corroborate this picture: nine PermaFrance boreholes (2800-4300 m a.s.l.) warmed by up to +1 °C at 10 m in a single decade and show active-layer thickening of ~2 m per decade, particularly after the anomalously warm summer of 2015 (Magnin et al., 2024); long-term Swiss PERMOS/SLF sites (1997-2019, 2500-3300 m a.s.l.) document depth-penetrating warming, lengthening zero-curtain periods and the strongest trends where ground-ice content is low (Haberkorn et al., 2021); Italian examples add detail, with Cime Bianche (3100 m a.s.l.) illustrating the dominant control of heterogeneous snow cover on subsurface temperatures (Pogliotti et al., 2015), while the 235 m SHARE-Stelvio core (~3000 m) shows that 20th century atmospheric warming has already propagated >150 m into bedrock (Pogliotti et al., 2015). Rock wall focused boreholes in the Mont Blanc massif (3160-4300 m) validate 2D conductive-latent-heat models that foresee permafrost loss on south-facing faces below ~3300 m by 2100, linking thermal degradation directly to future rock-fall potential (Magnin et al., 2017).

Several Alpine boreholes also host displacement sensors that tie this warming to incipient mechanical change. Inclinometer strings in 25 m shafts through the Furggwanghorn rock glacier (Valais) locate an active shear horizon at ~15 m depth, confirming internal deformation within warming, ice-rich debris (Merz et al., 2012). At a recently deglaciated slope above the Trift glacier, three boreholes equipped with thermistors and strain gauges register micrometre-scale, partially irreversible fracture opening events that coincide with warm-season pore-pressure peaks, implicating thermo-hydro-mechanical stress redistribution as a trigger for damage accrual (Hugentobler, Aaron and Loew, 2021). Together, these datasets establish that heat transport is affecting the strength of Alpine slopes, while integrated borehole measurements are required to capture the thermal and mechanical responses. Despite extensive monitoring efforts across the Alps, few studies have combined deep borehole displacement data with 3D DEM simulations to interpret thermo-mechanical processes at slope scale.

This paper aims at investigating the mechanical response of high-altitude rock slopes under resistance degradation. The research site at Capanna Margherita hut on Monte Rosa massif is described in Section 2. The Distinct Element model (DEM) of the rock slope is introduced and defined in Section 3. Numerical simulations, where varied properties of rock joints and bridges are considered, are described, and their results are compared to the borehole measurements in Section 4.

2 SITE DESCRIPTION

The case site is at Capanna Margherita hut, located at Punta Gnifetti of the Mont Rosa massif in Italy (Figure 1). At 4,554 meters above sea level, Capanna Margherita is the highest mountain hut and the highest structure in Europe. Due to its location just on the edge of a subvertical rock slope, and the

exceptionally, for the altitude, high temperature (above 0 °C) recorded at the hut for consecutive days in several recent summers, a series of research activities have been carried out there since 2019.

Capanna Margherita was initially built in 1893 and was completely renovated in 1980. The hut has a wooden structure and is covered by a copper outer shell. The main hut facade features an overhanging balcony and is parallel to a subvertical rock slope (dip direction N117°E, dip 80° - labelled as front slope in the following). On the contrary, the back slope is much gentler (about 45°) and is covered by a few meters thick ice. The hut rests directly on the nearly horizontal rock outcrop on top of Punta Gnifetti, while the balcony is supported by wooden posts.

Figure 1. Capanna Margherita hut.

A thorough survey reconstructed the geo-mechanical features of Punta Gnifetti, by using laser scanner, photogrammetry, and geo-radar, and by performing direct observation of visible discontinuities on the rock face. In particular, this survey returned the 3D point cloud of the summit and statistical joints sets data.

A series of preliminary DEM analyses have been performed based on the outcomes of the survey, at the rock joint and rock slope scales. However, the reliability of such numerical model is limited by incomplete data on joint conditions in depth (potential ice/water presence) and the lack of in-situ measurements for validation (Wang and Calvetti, 2021; 2022; Boffelli and Calvetti, 2023).

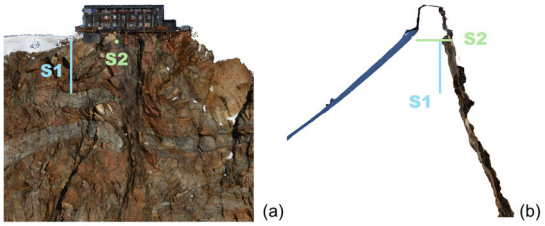

Figure 2. Borehole positions. (a) along N117°E; (b) along N27°E.

A new monitoring campaign started in 2023 whose initial setup and the analysis of the first available dataset were presented by Bai and Calvetti (2024). Two boreholes were drilled at Capanna Margherita, as shown in Figure 2: S1 is vertical and 20 meters deep, while S2 is horizontal and 10 meter deep. Borehole optical televiewer (OPTV) was used to map the orientations of planar features such as fractures and joints that intersect the boreholes. Crucially, the images of the borehole wall indicated that there is neither visible ice nor water in the observed joints.

Two multi-parametric monitoring columns (DMS) were installed in S1 and S2. DMS columns are made of 1 m long steel modules connected by reinforced rubber joints. Modules are equipped with inclinometer, thermometer, accelerometer, and digital compass. In particular, the first 8 meters in S2 and 15 meters in S1 are monitored. One piezometer (S1) and two fixed base extensometers (S2) complete the DMS setup.

3 DISTINCT ELEMENT MODEL

The numerical simulations are performed with the 3DEC code (Itasca). The geometry of the model closely reproduces the slope profile (Section 3.1). Considering the low stress level, and for the sake of simplicity, rock blocks are modelled as rigid elements. Then joint sets are introduced into the model considering multiple pieces of information, including interpretation of the 3D point cloud and direct OPTV observation in boreholes (Section 3.2).

The simulations are conducted by following a strength reduction technique, where joint resistance is progressively decreased until the failure of the hut is provoked.

3.1 *Geometry*

The process of defining the initial geometry is shown in Figure 3. Starting from the point cloud, a range of 100x100x100 meters was selected (Figure 3(a)) and was transferred to a STL file which represents the surface geometry. The selected range ensures a sufficient distance between the boundaries and the area of interest and previous analyses by Boffelli (2022) showed that further enlargement caused negligible variations in the results. The bottom and lateral sides are added to compose a closed volume and provide boundary conditions (Figure 3 (b)). The rigid block model in 3DEC is generated from the imported STL file (Figure 3 (c)). It is worth noting that the hut is represented by a rigid element with the same size and weight of the hut, which allows to check its stability during the simulations. This representation is appropriate because the hut rests directly on the rock surface without an embedded foundation, and full structure-rock interaction analysis is not required. Its displacement and velocity were tracked to verify stability during the simulations.

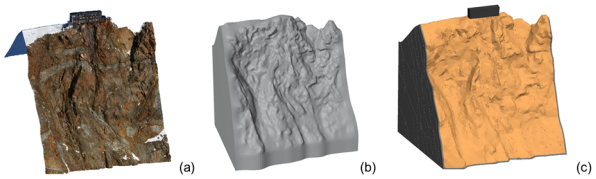

Figure 3. The process of generating model geometry. (a) Point cloud; (b) Closed STL; (c) 3DEC model.

3.2 *Joints setting*

Table 1. Average properties of joint families.

Joint set	Colour	Dip direction (°)	Dip (°)	Spacing (m)
A		90	85	4.1
B		43	76	7.4
C		172	82	8.1
D		309	56	10.8
E		160	48	3.4
F		139	81	4.7
G		77	53	2.9
H		120	62	1.4

The joints set introduced in the model were based on statistical results from geo-mechanical analysis (average values are reported Table 1) and are integrated with the OPTV data from boreholes. The position of some specific joints, namely those clearly visible on the slope surface, was precisely assessed and reproduced in the model, also thanks to a point cloud analysis

with detection of joint planes adopting the Hough method (Boulch and Marlet, 2016), as shown in Figure 4. To avoid the unrealistic generation of perfectly planar and regular joints, a random deviation of 2.5° is applied to the dip and dip direction of each joint (Boffelli and Calvetti, 2023).

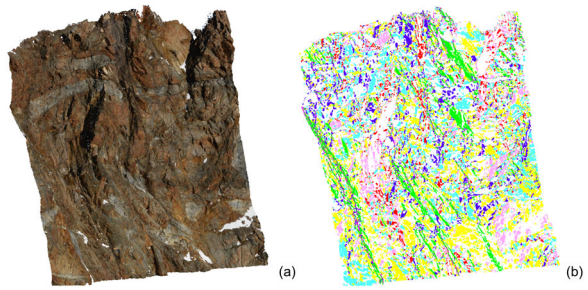

Figure 4. Point cloud (a) and surface planes filtered by their normal (b).

In addition to the joints detected from the surface interpretation, the open joints observed in boreholes were introduced in the model at the corresponding positions. The dip and dip direction of joints detected in the boreholes are shown in Figure 5, where labels A, D and G refer to the families reported in Table 1. As a matter of fact, only few borehole joints belong to the surface joints (Table 1), which suggests that they can be considered as local fractures. Therefore, in the model these joints extend just within a 5-meter diameter range from the borehole axis.

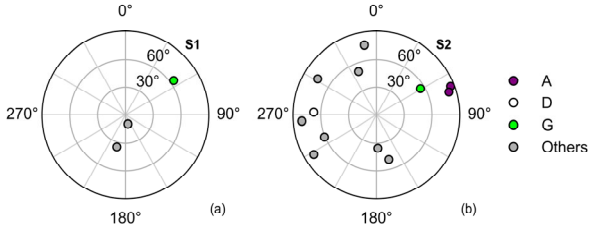

Figure 5. Schmidt plot of joints detected in boreholes (a) S1; (b) S2.

The outcome of the generation procedure is shown in Figure 6. The model is made of approximately 80000 blocks. It is worth noting that rigid block DEM models require joints to be geometrically continuous (fully persistent) to allow relative displacements between adjacent blocks. Therefore, the reproduction of real joint persistence has to be achieved through appropriate choices regarding joint resistance (see Section 3.3).

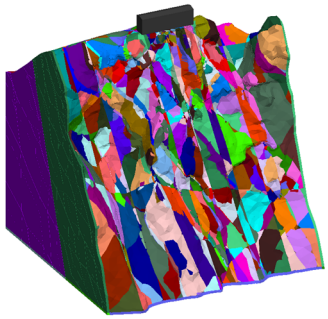

Figure 6. 3DEC model with joints, blocks are coloured randomly.

3.3 *Model parameters*

In a rigid block model, required parameters are block density, joint resistance and joint stiffness (Table 2). The adopted rock density, cohesion and tensile resistance, and joint elastic stiffness, are typical values for the paragneiss and orthogneiss units that compose the rock mass.

Joint friction - considering low geostatic stresses acting just below the mountain peak and close to the main slope - is not expected to play a significant role compared to that of joint cohesion and tensile resistance. The adopted value is based on direct observation of joint roughness.

Table 2. Model parameters.

Parameter	Symbol	Value	Unit
Rock density	ρ	2650	kg/m^3
Joint normal stiffness	kn	1	GPa
Joint shear stiffness	ks	0.5	GPa
Joint friction angle	Φ	40	°
Joint persistence	K	0-97.5	%
Rock bridge cohesion	c	30	MPa
Rock bridge cohesion (residual)	c_r	0-30	MPa
Rock bridge tensile resistance	t	15	MPa
Rock bridge tensile resistance (residual)	t_r	0	MPa

In general, the overall cohesive (tensile) resistance available along a joint depends on joint persistence and rock bridge properties. For example, the equivalent joint cohesion, $\bar{c}$, can be evaluated as (Jennings, 1970):

$$\bar{c} = c \cdot (1 - K) \quad (1)$$

where c is rock bridge cohesion and K is joint persistence. A similar relation exists for tensile resistance.

The approach adopted in 3DEC is characterised by the following points:

- joints are geometrically continuous.
- the faces of blocks are triangulated, and sub-contacts are created at adjacent block faces in correspondence to triangle vertices.
- when persistence K is specified, only a percent of sub-contacts, $1 - K$, is given rock bridge properties (cohesion and tensile resistance).

The geometric distribution of rock bridge sub-contacts along any joint is randomly generated by 3DEC. Note that the numerical model here adopted has approximately 675000 sub-contacts, which justifies this statistical approach.

From Equation (1), it is clear that the same equivalent joint resistance can be attained with different combinations of rock bridge cohesion (and tensile resistance) and persistence. One of the goals of DEM model is to verify whether the failure of the slope is just depending on equivalent joint resistance, or persistence and rock bridge resistance play individual roles. In other terms, this means verifying whether Equation (1) is valid at the slope scale. This issue is particularly relevant to numerical modelling because it is difficult to assess the value of persistence from in-situ observations.

In this research, values of joint persistence, defined as the percentage of sub-contacts without rock-bridge properties, were varied from 0 to 97.5% as part of the parametric study. As a reference, Boffelli and Calvetti (2023) estimated persistence between 96% and 98% for the rock mass at Capanna Margherita. Note that bridge tensile resistance is assumed to be half of bridge cohesion; unless otherwise specified, in the following we are referring to cohesion only to describe the results. Furthermore, various types of post peak behaviour, from ductile to fragile, are studied by varying the residual

cohesion; residual tensile resistance is always zero (see Table 2).

4 SIMULATION RESULTS

4.1 *Simulation procedure*

First, a series of models are created with different values of joint persistence and gravity force is applied in order to generate the initial state of stress in the joints. Then, for each model, rock bridge resistance is progressively reduced until a major failure - involving the hut - is triggered. The limit values of rock-bridge cohesion, and the corresponding equivalent joint cohesion (Equation (1)) are labelled as critical (see Section 4.4).

4.2 *Qualitative comparison with in-situ measurements*

The trajectory of relative displacements between the surface and the deep ends of DMS columns is shown in Figure 7 for the period from 2023/10/10 to 2024/06/29 (when instruments were damaged by a lightning storm). The trajectories of both columns were plotted by cumulating the relative displacements along each column with respect to their deep ends, which were assumed to be fixed (zero displacement). The vertical borehole trajectory is projected on the horizontal plane, while the horizontal borehole trajectory is projected on a vertical plane, which is virtually coincident with the rock slope (L and R correspond to N207°E and N27°E, respectively; U and D stand for upwards and downwards, respectively).

The movement in S1 tends towards N305°E, i.e. approximately towards the back slope (N297°E) and tends to stabilise at the end of the considered period. As to S2, the movement is mainly vertical, initially (winter and early spring) downwards, then upwards. The maximum recorded displacements are about 7 and 3 mm, respectively.

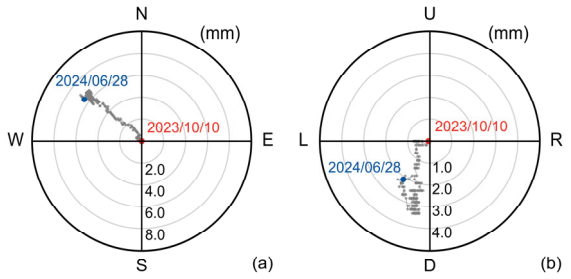

Figure 7. Trajectories of columns in boreholes. (a) S1; (b) S2.

The displacements in the model at the positions corresponding to that of the DMS columns are qualitatively compared with in-situ measurements (maximum values) in Figure 8. The comparison focuses on displacement directions and relative behaviour rather than absolute magnitudes, to evaluate whether the observed movements can be attributed to rock-mass degradation. Model displacements are projected on N297°E for S1 and on the vertical plane for S2. Model displacements are provoked by the progressive decrease in rock-bridge cohesion; those reported here correspond to the last stable reduction step, just before critical cohesion is attained, for various combinations of joint persistence and residual to peak cohesion ratio (respectively K and R in the legend). Notably, higher joint persistence K results in smaller relative displacements along both columns just before failure, generally. This occurs because low-persistence settings promote a more gradual failure that mobilises deeper rock layers. In contrast, high-persistence joints favour a failure mechanism confined to the shallower rock mass, within the depth interval of the DMS columns. Details are further discussed in Section 4.3.

Qualitatively, the model reproduces the observed displacement at S2 reasonably well, with both showing a downward movement trend. In contrast, the displacement direction at S1 in the model appears opposite to that observed in the field, suggesting that the movement at S1 may not be primarily mechanically driven.

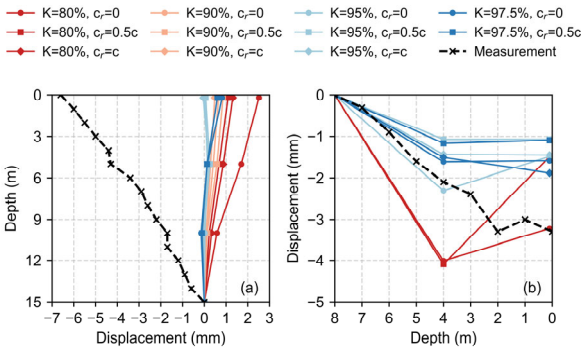

Figure 8. Displacement profiles from measurement and simulations. (a) vertical borehole; (b) horizontal borehole.

This interpretation is consistent with the strong correlation between the evolution of displacements and of temperature at S1 (Figure 9 (a)). In particular, the displacement at S1 shows a strong linear relationship with temperatures measured in depth (at –6, -11 and -15 m from the surface), while the correlation with near-surface temperature is much weaker. In this respect, it is worth noting that Bai and Calvetti (2024) have shown that there is a significant time lag between shallow and deep temperature variations.

As to S2, the displacement shows poor correlation with temperature (Figure 9 (b)), which aligns with previous modelling results suggesting that the movement can be the combined outcome of mechanical and thermal effects, with the latter being responsible for the upward trend.

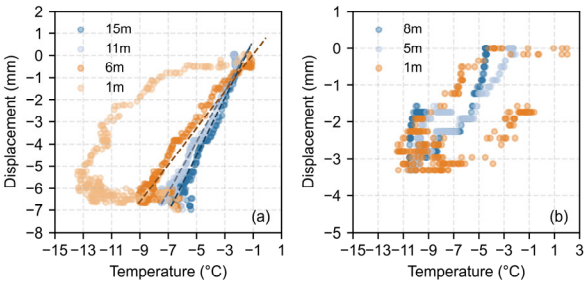

Figure 9. Relationship between cumulative displacement with temperature recorded in different depths. (a) S1, displacement along N125°E; (b) S2, displacement in vertical direction.

4.3 *Failure kinematics*

The displacement field along the cross-section oriented N117°E – N297°E (perpendicular to the front slope) at the hut, is shown for models with joint persistence values of 90% (Figure 10), 95% (Figure 11), and 97.5% (Figure 12). In each figure, the displacement magnitudes at critical stage and after failure are compared for two cases: $c_r = 0$ (subplots (a) and (b)), and $c_r = c$ (subplots (c) and (d)). Since post-failure displacements are progressively increasing, those recorded after 1000 calculation steps are reported here.

Overall, neither the joint persistence K nor joint ductility has a big influence on the failure mechanism. The failure is mainly occurring in a relatively shallow zone, whose extension just slightly smaller for the fragile model, which contributes to

the collapse near the hut. However, persistence does slightly affect the extent of the unstable region: as the persistence increases, the involved volume becomes smaller and the displacement magnitude at the critical state decreases.

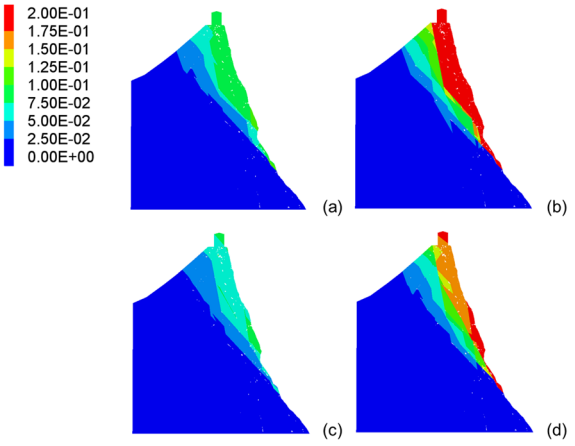

Figure 10. Displacements magnitude, K =90%. c_r =0: (a) at critical cohesion, (b) incipient failure; $c_r = c$: (c) at critical cohesion, (d) incipient failure.

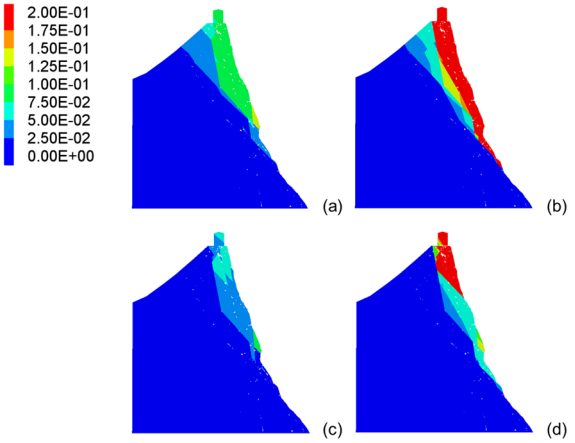

Figure 11. Displacements magnitude, K=95%. c_r =0: (a) at critical cohesion, (b) incipient failure; $c_r = c$: (c) at critical cohesion, (d) incipient failure.

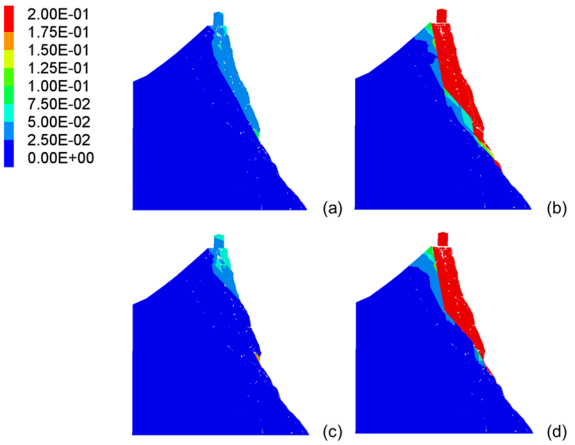

Figure 12. Displacements magnitude, K=97.5%. c_r=0: (a) at critical cohesion, (b) incipient failure; $c_r = c$: (c) at critical cohesion, (d) incipient failure.

4.4 *Influence of persistence on critical cohesion*

The critical rock-bridge cohesion for each model is shown in Figure 13 (a). The corresponding equivalent critical joint cohesion $\bar{c}$ is calculated using Equation (1) and shown in Figure 13 (b).

As expected from the definition of equivalent cohesion, the critical rock-bridge cohesion increases with persistence, and is larger when residual cohesion is zero. However, the relationship between rock-bridge critical cohesion c and persistence K is not inversely proportional, as one would expect from Equation (1). This is also evident from the value of $\bar{c}$, which vary for different levels of K. This suggests that the linearity between $\bar{c}$ and K does not translate to the slope scale, where block interactions and slope-scale kinematics disrupt the simple mixture assumption implicit in Equation (1).

Nonetheless, the influence of persistence on critical equivalent joint cohesion tends to disappear for K larger than 80% (ductile model) and 95% (fragile model). Therefore, provided K is assumed in the realistic range for the slope under consideration (and for similar conditions, which are quite common), i.e. above 95%, Figure 13 shows that the initial choice of persistence in the DEM model does not significantly affect the outcome. In other terms, under these conditions, small uncertainties in the estimated persistence are unlikely to compromise the reliability of the simulation results.

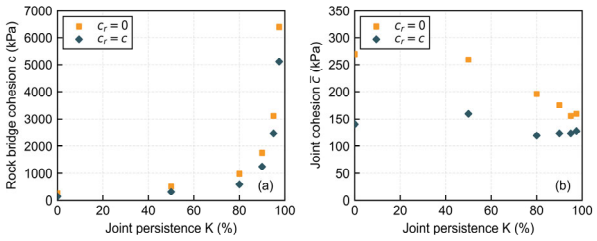

Figure 13. Cohesion values at failure. (a) Rock bridge cohesion; (b) equivalent joint cohesion.

5 CONCLUSION

This research allowed to get useful information both regarding the modelling choices involved in the numerical DEM analysis and the interpretation of in-situ data. The results indicate that, for the slope conditions considered, joint persistence and ductility have only a limited influence on the overall failure mechanism. While increasing persistence slightly reduces the extent of the unstable zone and lowers critical-state displacements, the collapse consistently develops within a shallow zone under the hut. The comparison with in-situ displacement measurements suggests that movements at S2 can be partly reproduced by mechanical degradation of the rock mass, whereas displacements at S1 are likely dominated by thermally induced processes. Additionally, the individual role of rock bridge cohesion and joint persistence in determining the rock mass resistance has been highlighted. However, this affect decreases with K and can be neglected within the realistic range of persistence.

Further developments could improve the model by introducing spatial variability in the persistence setting, for example assigning higher values to the near surface rock mass which is more fractured, and lower values at depth for more intact rock. Moreover, extending the current purely mechanical framework to a thermo-mechanical coupled approach would enable a more comprehensive comparison with monitoring data, offering deeper insight into distinguishing the reversible and irreversible deformation in high altitude rock slopes under global warming conditions.

6 ACKNOWLEDGEMENTS

This research is supported by a China Scholarship Council grant awarded to Yunlu Bai and by the Italian Alpine Club (CAI). The authors acknowledge the contribution to the installation of the sensors at Capanna Margherita by Fabio Baio, Daniele Bernasconi, Tore Panzeri and Elia Negrini. The technical support by Luigi Foglino is also gratefully acknowledged.

7 REFERENCES

Bai, Y. and Calvetti, F., 2024. Monitoring of Global Warming Effects in High Alps. The 9th International Conference on Civil, Structural and Transportation Engineering. https://doi.org/10.11159/iccste24.209.

Boffelli, W., 2022. Numerical Modelling of Global Warming Effects on The Stability of Rock Faces in High Alps. Master's Thesis. Politecnico di Milano. https://hdl.handle.net/10589/195973

Boffelli, W. and Calvetti, F., 2023. DEM Modelling of Rock Masses Affected by Permafrost Degradation. The 8th International Conference on Civil, Structural and Transportation Engineering. https://doi.org/10.11159/iccste23.212.

Boulch, A. and Marlet, R., 2016. Deep Learning for Robust Normal Estimation in Unstructured Point Clouds. *Computer Graphics Forum*, 35(5), pp.281–290. https://doi.org/10.1111/cgf.12983.

Guglielmin, M., Donatelli, M., Semplice, M. and Serra Capizzano, S., 2018. Ground surface temperature reconstruction for the last 500 years obtained from permafrost temperatures observed in the SHARE STELVIO Borehole, Italian Alps. *Climate of the Past*, 14(6), pp.709–724. https://doi.org/10.5194/cp-14-709-2018.

Haberkorn, A., Kenner, R., Noetzli, J. and Phillips, M., 2021. Changes in Ground Temperature and Dynamics in Mountain Permafrost in the Swiss Alps. *Frontiers in Earth Science*, 9. https://doi.org/10.3389/feart.2021.626686.

Hugentobler, M., Aaron, J. and Loew, S., 2021. Rock Slope Temperature Evolution and Micrometer-Scale Deformation at a Retreating Glacier Margin. *JOURNAL OF GEOPHYSICAL RESEARCH-EARTH SURFACE*, 126(11). https://doi.org/10.1029/2021JF006195.

Magnin, F., Deline, P., Ravanel, L., Noetzli, J. and Pogliotti, P., 2015. Thermal characteristics of permafrost in the steep alpine rock walls of the Aiguille du Midi (Mont Blanc Massif, 3842 m a.s.l). *The Cryosphere*, 9(1), pp.109–121. https://doi.org/10.5194/tc-9-109-2015.

Magnin, F., Josnin, J.-Y., Ravanel, L., Pergaud, J., Pohl, B. and Deline, P., 2017. Modelling rock wall permafrost degradation in the Mont Blanc massif from the LIA to the end of the 21st century. *The Cryosphere*, 11(4), pp.1813–1834. https://doi.org/10.5194/tc-11-1813-2017.

Magnin, F., Ravanel, L., Bodin, X., Deline, P., Malet, E., Krysiecki, J. and Schoeneich, P., 2024. Main results of permafrost monitoring in the French Alps through the *PermaFrance* network over the period 2010–2022. *Permafrost and Periglacial Processes*, 35(1), pp.3–23. https://doi.org/10.1002/ppp.2209.

Merz, K., Rabenstein, L., Buchli, T. and Maurer, H., 2012. Geophysical Characterization of the Furggwanghorn Rock Glacier, Switzerland. 74th EAGE Conference and Exhibition - Workshops. Copenhagen, Denmark. https://doi.org/10.3997/2214-4609.20149782.

Noetzli, J., Isaksen, K., Barnett, J., Christiansen, H.H., Delaloye, R., Etzelmüller, B., Farinotti, D., Gallemann, T., Guglielmin, M., Hauck, C., Hilbich, C., Hoelzle, M., Lambiel, C., Magnin, F., Oliva, M., Paro, L., Pogliotti, P., Riedl, C., Schoeneich, P., Valt, M., Vieli, A. and Phillips, M., 2024. Enhanced warming of European mountain permafrost in the early 21st century. *Nature Communications*, 15(1), p.10508. https://doi.org/10.1038/s41467-024-54831-9.

Pogliotti, P., Guglielmin, M., Cremonese, E., Morra Di Cella, U., Filippa, G., Pellet, C. and Hauck, C., 2015. Warming permafrost and active layer variability at Cime Bianche, Western European Alps. *The Cryosphere*, 9(2), pp.647–661. https://doi.org/10.5194/tc-9-647-2015.

Ravanel, L., Magnin, F. and Deline, P., 2017. Impacts of the 2003 and 2015 summer heatwaves on permafrost-affected rock-walls in the Mont Blanc massif. *Science of The Total Environment*, 609, pp.132–143. https://doi.org/10.1016/j.scitotenv.2017.07.055.

Wang, G. and Calvetti, F., 2021. DEM Modelling of Ice Filled Rock Joints. In: M. Barla, A. Di Donna and D. Sterpi, eds. *Challenges and Innovations in Geomechanics*, Lecture Notes in Civil Engineering. Cham: Springer International Publishing. pp.941–948. https://doi.org/10.1007/978-3-030-64518-2_112.

Wang, G. and Calvetti, F., 2022. 3D DEM investigation of the resistance of ice and frozen granular soils. *European Journal of Environmental and Civil Engineering*, 26(16), pp.8242–8262. https://doi.org/10.1080/19648189.2021.2021997.